International Journal of Mechanical, Industrial and Aerospace Sciences
ISSN: 2517-9950
Vol:4, No:11, 2010

Transient Thermal Modeling of an Axial Flux Permanent Magnet (AFPM) Machine Using a Hybrid Thermal Model

J. Hey[1], D. A. Howey [1], R. Martinez-Botas[1], M. Lamperth[2]

Abstract**—**This paper presents the development of a hybrid thermal model for the EVO Electric AFM 140 Axial Flux Permanent Magnet (AFPM) machine as used in hybrid and electric vehicles. The adopted approach is based on a hybrid lumped parameter and finite difference method. The proposed method divides each motor component into regular elements which are connected together in a thermal resistance network representing all the physical connections in all three dimensions. The element shape and size are chosen according to the component geometry to ensure consistency. The fluid domain is lumped into one region with averaged heat transfer parameters connecting it to the solid domain. Some model parameters are obtained from Computation Fluid Dynamic (CFD) simulation and empirical data. The hybrid thermal model is described by a set of coupled linear first order differential equations which is discretised and solved iteratively to obtain the temperature profile. The computation involved is low and thus the model is suitable for transient temperature predictions. The maximum error in temperature prediction is 3.4% and the mean error is consistently lower than the mean error due to uncertainty in measurements. The details of the model development, temperature predictions and suggestions for design improvements are presented in this paper.

Keyword**—**Electric vehicle, hybrid thermal model, transient temperature prediction, Axial Flux Permanent Magnet machine.

I. Introduction

THE demand for high power density and efficient energy conversion devices has been rising because of the growing awareness of the need for cleaner technology in many industries. One such device is the Axial Flux Permanent Magnet (AFPM) machine which has a much higher power density as compared to the conventional and more widely used radial flux machines [1]. AFPM is used in applications ranging from wind turbines for electricity generation to hybrid electric vehicles for propulsion power [2]. The maximum efficiency of the typical AFPM is in the range of 90 to 97% [3]. The efficiency of the AFM140 machine (Fig. 1) developed by EVO Electric has a maximum efficiency of 96.5%.

The energy loss in such a device is mainly in the form of heat generation in the copper coils, stator and magnets [4]. The copper winding of the stator coils heats up because of resistive heating. Additionally, undesirable eddy currents flow in the stator core and magnets causing heat generation. The repeated magnetization and demagnetization of the ferromagnetic materials within the machine means that energy is loss due to hysteresis that is inherently present in such a process.

[1] Mechanical Engineering Department, Imperial College, Exhibition Road, South Kensington, London SW7 2AZ, UK.
[2] Evo Electric Ltd,14 Woking Business Park, Woking, GU21 5JY, UK.

Fig. 1 EVO Electric AFM140 Machine

The heat generation depends on the machine's operating conditions such as the torque demand and rotation speed. The resistive heating is largely dependent on the current flowing through the copper coils which is proportional to the torque in the machine. The friction between the rotor and fluid also causes heat generation because of viscous forces [5]. Mechanical losses at the bearings are also substantial especially at high rotation speeds. These sources of heat generation are inevitable in any rotating electromagnetic device.

The heat generation causes an increase in the temperature of the machine which affects its performance and reliability which would be further elaborated in the subsequent sections. As heat generation is concentrated in the copper coils, the temperature rise is expected to be largest at the coils and the surrounding stator core. The maximum temperature recorded in the EVO Electric AFM140 machine is about 160°C for a 50 overload condition with forced liquid cooling around the casing. The magnet and rotor also experiences substantial rise in temperature because of eddy current and hysteresis losses though no exact data is available because of the difficulty in measuring the temperature of a rotating component. High temperature is undesirable because it damages the delicate insulation material surrounding the coils and it also impairs the magnetic properties of the magnets [4].

TABLE I
NOMENCLATURE

$[C]$	Thermal capacitance matrix (J/K)	$\bar{h}$	Average heat transfer coefficient (W/m^2-K)
$[K]$	Thermal conductance matrix (W/K)	$\overline{q'}$	Average heat flux (W/m^2)
$\{T\}$	Temperature vector (K)	$\overline{T_s}$	Average surface temperature (K)
$\{P_l\}$	Total losses vector (W)	$P_{l,c}$	Copper losses (W)
$\dot{q}$	Heat transfer (W)	$P_{l,e}$	Eddy losses (W)
R_{cd}	Thermal conduction resistance (K/W)	$P_{l,\mathrm{h}}$	Hysteresis losses (W)
R_{cv}	Thermal convection resistance (K/W)	$P_{l,\mathrm{b}}$	Bearing losses (W)
T_1	Temperature of element 1 (K)	$P_{l,\mathrm{w}}$	Windage losses (W)
T_2	Temperature of element 2 (K)	$P_{l,\mathrm{m}}$	Total mechanical losses (W)
T_f	Temperature of the fluid (K)	R_o	Resistance of copper at 20°C
k	Thermal conductivity (W/m-K)	T_c	Temperature of the copper winding (°C)
h	Heat transfer coefficient (W/m^2-K)	I_{rms}	RMS current in the copper winding (A)
A	Contact area for heat transfer (m^2)	a,b	Geometric and material correction factor
l	Heat transfer path length (m)	B	Magnetic flux density (Wb)
L	Axial length of annulus section or cylinder (m)	m,n	Power factor for magnetic flux density
θ	Angle of annulus section (rad)	M	Mass of rotor (kg)
k'	Thermal conductance coefficient (W/m^2-K)	$\{C\}'$	Inverse of thermal capacitance matrix (K/J)
t	Thickness of interface material (m)	$e_{\%}$	Percentage error
V_t	Average tangential velocity (m/s)	$\bar{e}_{\%}$	Mean value of error
A_{eq}	Equivalent cross sectional area (m^2)	T_{sim}	Simulated temperature (°C)
ρ	Density of air (kg/m^3)	T_{exp}	Experimental temperature (°C)
c_p	Specific heat capacity of air (J/kg)	N	Total number of time step
δt	Simulation time step (s)		

The breakdown of insulation material would result in a catastrophic failure of the machine while a heated magnet would result in the reduction of magnetic field strength and hence lower power output. Adverse temperature of the magnet would also cause irreversible loss of the magnet strength [6]. All these problems are unwanted and much has to be done to prevent the motor from reaching predetermined critical temperatures based on the component material limits.

Therefore, there is a strong need to understand the mechanisms of heat transfer and also develop abilities for temperature prediction [7]. An understanding of the heat transfer process would lead to better cooling technology and hence better designed machines [8]. Temperature prediction is equally important because it allows for analysis of the machine as it is put through its typical operation cycle or even determining the optimum operating point and the point of failure due to thermal overload. All these are compelling reasons for the subsequent transient thermal modeling work that would be presented in this paper.

II. THERMAL MODELING

A. Machine Component and Geometry

As a case study for the thermal modeling methodology proposed in this paper, the EVO Electric AFM 140 is selected as a test case. The machine specifications and dimensions are given in Table II. The main machine components and geometry is shown in the schematic drawing in Fig. 2. The model developed here only covers a sector of half the machine axially because there is symmetry of the motor in the mid plane across the cross section and each sector repeats itself after every 7.2 degrees of revolution about the motor axis.

TABLE II
EVO AFM140 specifications

Motor Parameters	Value (Units)
Nominal Continuous Torque	220Nm
Nominal Power @ 3250 rpm	75kW
Torque Density	10Nm/kg
Power Density	4.2kW/kg
Peak Efficiency	96.5%
Diameter	380mm
Length	115.2mm
Weight	40kg

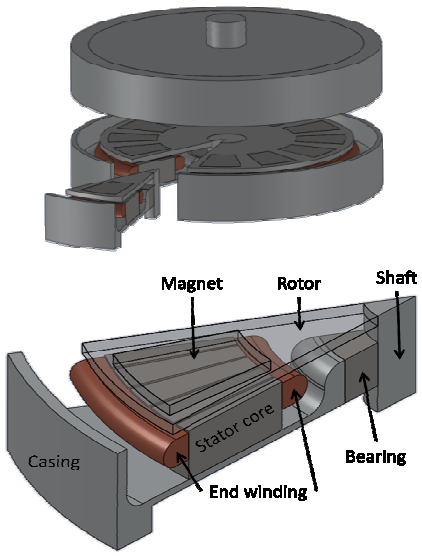

Fig. 2 Schematic drawing of the EVO AFM140

The main components of the motor are the rotor disc with permanent magnets embedded in it and the electromagnetic stator with copper windings coiled around a ferromagnetic steel core. There is a small air gap of about 3mm between the rotor and stator surface as shown in the sectional view in Fig. 3. The copper coils are bundles of individual wires of diameter 0.5 mm based on the American Wire Gauge standard (24 AWG) which is no shown in the illustration. The exterior of the motor casing is cooled by passing water through cooling channels embedded in the casing which is not used in the current investigation.

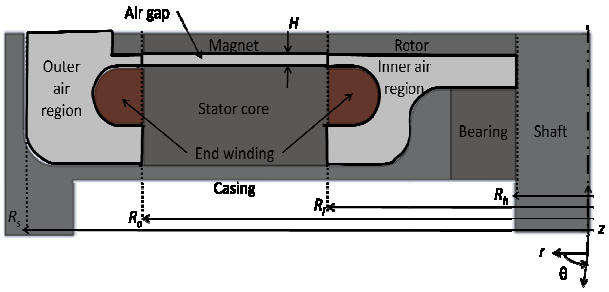

Fig. 3 Sectional view of the EVO AFM140 at the mid plane

B. Model Development

A hybrid lumped parameter and finite difference model is developed to investigate the heat transfer process in the EVO AFM140 machine. The approach is based on discretising the motor component into small elements. The conservation of energy at each element gives rise to (1). $[C]$ and $[K]$ are *m x m* matrix of the heat capacitance and thermal conductance of the paths connecting the elements respectively. *m* is the number of elements or temperature nodes while $\{P_l\}$ is the total losses vector and $\{T\}$ is the temperature vector which has dimensions equal to *m*.

$$[C]\{\dot{T}\} = [K]\{T\} + \{P_l\} \quad (1)$$

The temperature change of each element is described by the balance of the losses generated and net heat flow in or out of the element which is described by the terms on the right hand side of (1). The rate of change of temperature depends on its heat capacity and the net heat gained by the element. In the proposed method, the element can be of arbitrary shape and size. This allows for a better fit of the elements with the specific geometry of the component. It is different from the finite element methods because the elements in the latter method are described by regular pyramid, tetrahedral or hexagonal elements.

To ensure consistency, each of the motor components is separated into a regular grid of nodes. For example, the copper windings are discretised into cylinders while the casing is cut into small sections of an annulus. The number of nodes for each component depends on the geometry of the component and spatial resolution required. The details of the number of nodes for each component are listed in Table III.

TABLE III
NUMBER OF TEMPERATURE NODES

Component	Number of Nodes	Shape of element
Stator	30	Annulus section
Copper Winding	672	Cylinders
Casing	7	Annulus section
Rotor and magnet	3	Annulus section
Bearing and Shaft	4	Annulus section
Air cavity	1	Control volume
Total	717	

The general formulation of the governing equation has been pioneered in work such as those by Mellor et. al. [9]. The details of the formulation can be found in publications listed in the references [10], [11]. A brief outline of the formulation process would be presented here for easier discussion of the method thereafter.

The heat capacitance matrix $[C]$ and thermal conductance matrix $[K]$ is derived from the dimensions, material and thermal property of each element. The heat flow in or out of an element is determined by the linear heat conduction and convection equation while radiation heat transfer is neglected in this model. The heat conduction and convection equations are presented below in (2) and (3) respectively.

$$\dot{q} = -\frac{1}{R_{cd}}(T_2 - T_1) \quad (2)$$

$$\dot{q} = -\frac{1}{R_{cv}}(T_1 - T_f) \quad (3)$$

Where

$$R_{cd} = \frac{l}{kA} \quad (4)$$

$$R_{cd} = \frac{\ln(\frac{r_o}{r_i})}{\theta Lk} \quad (5)$$

$$R_{cd} = \frac{1}{4\pi Lk} \quad (6)$$

$$R_{cv} = \frac{1}{hA} \quad (7)$$

A is the contact area where heat transfer occurs. *l* is the length of the heat transfer path. r_o and r_i are the outer and inner radius of the annulus section respectively. *L* is the axial length of the annulus section or cylinder. θ is the angle of the annulus section. The key dimensions of the typical elements are shown in Fig. 4. These parameters differ for different element shape and it would be further elaborated below.

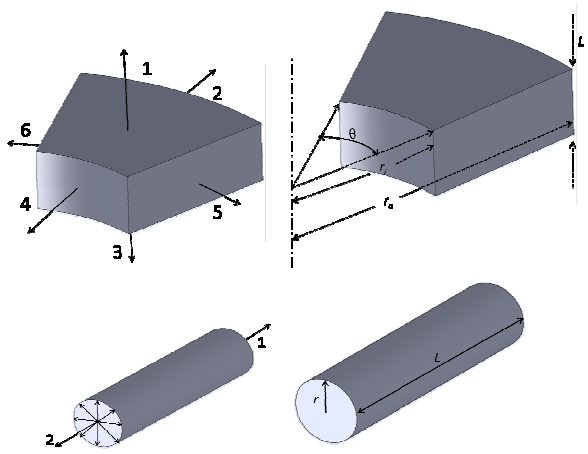

Fig. 4 Direction of heat transfer and key dimensions of the elements

The general element in the model can be represented by an annulus section or cylinder as shown in Fig. 4. The arrows show the directions of the heat transfer path for each element. Equation (4) would be used to calculate the conduction thermal resistance for flat surfaces such as face 1, 3, 5 and 6 of the annulus section and face 1 and 2 of the circular tube. Equation (5) would be used for circular surfaces such as the face 2 and 4 of the annulus section. Equation (6) would be used to work out the thermal resistance across the radial direction of a cylinder [12]. Equation (7) would be used to calculate the thermal resistance of any surface that is in contact with fluid.

The direction and magnitude of heat flow is driven by the temperature difference between the two points and the thermal resistance between them. The elements within the same grid are connected together in a regular thermal resistance network in all three dimensions of the grid. The thermal resistance networks for each component are then connected together by another set of thermal resistance which describes the interface connections. Another set of thermal resistances defines the heat transfer at the boundaries to the fluid. Eventually, the elements are linked together by these thermal resistances which represent all the physical connections.

The underlying assumption in this method is that heat transfer of each element in the different directions is independent of each other and can be decoupled for the selected range of element size. Secondly, the heat transfer can be sufficiently described by the first order linear heat transfer equation given by (2) and (3). The results will show that these assumptions do not affect the accuracy of the temperature by a large margin while at the same time simplifying the mathematical complexity of the model.

C. Model Parameters

1. Thermal Interface Connections

The conductance coefficient (*k'*) is a measure of the effectiveness of an interface boundary between two materials to transmit heat across this boundary. The ease of heat transfer is dependent on this coefficient and it may be due to the presence of an interface material or simply just the imperfect contact between the two surfaces. If an interface material is present, the effective conductance coefficient (*k'*) at the interface can be derived based on its thickness (*t*) and thermal conductivity (*k*) as shown in (8).

$$k' = \frac{k}{t} \tag{8}$$

However, some of the interface boundaries do not have an interface material. There is resistance to heat flow due to the imperfect contact between these components. The conduction coefficient of such an interface is a highly complex function of surface roughness and contact pressure. Therefore, average values of thermal conductance coefficients are used in these cases and it is based on the work done by Staton et. al. [8].

For example, the copper windings are insulated with mica typically. Mica has a thermal conductivity of about 0.25 W/m-K and the thickness of the mica insulation is 0.2mm in this machine. This works out to be an equivalent conduction coefficient of 1250 W/m^2-K. Similarly, the interface boundary between the copper windings and the stator has an effective conductance coefficient of 1440W/m^2-K due to the presence of an insulation sheet at the interface boundary. A list of the values for the different thermal conductance coefficient and their location is shown in Table IV [8], [12].

TABLE IV
LIST OF CONDUCTION COEFFICIENT

Location	Material Type	Conduction Coefficient (W/m^2-K)
Winding – Stator	Thermal Insulation	1440
Winding – Insulation	Mica	1250
Stator – Casing	Thermal Interface	80000
Magnet / Shaft – Rotor	Metal and Glass Fiber	4500
Casing – Bearing	Aluminum	7100

2. Computational Fluid Dynamics

Several pioneering work has been done to investigate the complex nature of air flow in an enclosed cavity with a stationary boundary on one side and rotating boundary on the other. As presented by Eric et. al. [13], there is clear evidence of circulating flow throughout such an enclosed cavity in the radial direction.

However, there is little numerical or experimental work done on modeling the flow dynamics in complex enclosed cavities like the one found in the EVO AFM 140 machine. Much work has been done to obtain accurate models and experimental data of fluid flow in similar cavities but with through flow such as the work done by Howey et. al. [14]. The nature of through flow and enclosed flow are expected to be very different. Thus much of these works would not be directly applicable to the current investigation.

Therefore, there is a need to do a comprehensive CFD simulation of the fluid flow dynamics and heat transfer. A conjugate heat transfer analysis is done using ANSYS CFX to investigate the fluid dynamics and heat transfer as a coupled

problem. Analysis of the fluid motion shows that the rotational momentum imparted to the air by the rotor is moving the air mostly in the tangential direction as shown in Fig. 5.

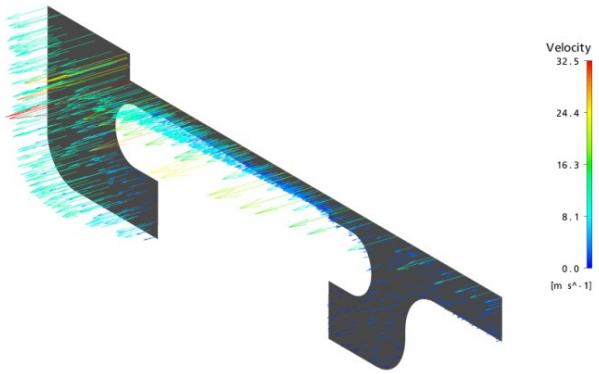

Fig. 5 Tangential velocity at the mid plane

At the same time, centrifugal force is pushing the air radially outwards as it is rotating with the rotor as shown in Fig. 6. It can be seen that the air is circulating within the entire air cavity though with some difficulty because of the restrictive geometry. There is localized circulation of the air in several regions in the air cavity namely in the air gap, outer and inner region.

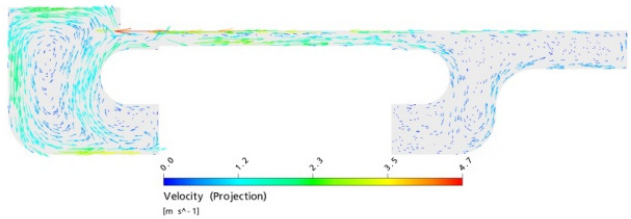

Fig. 6 Radial velocity at the mid plane

The average tangential velocity component across the mid plane is about 4.8m/s while the average radial velocity is just under 0.4m/s. It is an order magnitude lower and so it is reasonable to conclude that the bulk motion of the air particle is in the tangential direction. The presentation of the fluid motion has been simplified in this paper but it would be sufficient to give a good idea about how it affects the heat transfer to and from the fluid.

However, the task of calculating or measuring the heat transfer coefficient is not a trivial process. The focus of this paper is not on this specific area. The preceding discussion on the fluid dynamics provides the basis for some of the assumptions and simplifications used in developing the hybrid thermal model.

The CFD analysis leads to the simplification of the fluid domain into a control volume in which an average velocity is applied to the inlet of the control volume. Having simplified the fluid dynamics, it is now possible to integrate the lumped fluid domain into the hybrid model. The control volume would appear as another element in the model with an equivalent thermal capacitance c_{air} given by Equation (9). V_t is the average tangential velocity while A_{eq} is the equivalent cross sectional area where the fluid is crossing. ρ and c_p are the density and specific heat capacity of air respectively while δt is the simulation time step.

$$c_{air} = V_t A_{eq} \rho c_p \delta t \tag{9}$$

This lumped fluid domain is essentially a moving mass of air being exposed to heat transfer at its boundaries. As in the lumped parameter method, the heat transfer at the boundary is more significant than the heat transfer within the element. The underlying assumption is that the lumped fluid element would have largely unchanged internal flow conditions as it progresses along the tangential direction as shown in the CFD simulation. The results from the CFD simulation are used to obtain the average values of heat transfer coefficient at several locations as shown in Fig. 7.

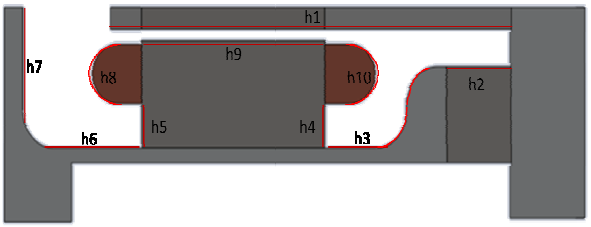

Fig. 7 Surface of interest and corresponding heat transfer coefficient

The values vary with the rotational speed. For the purpose of the work presented here, the rotation speed is set to a speed of 2000 rpm. Area averaged values of heat transfer coefficient $(\bar{h})$ are derived from the average surface heat flux $(\bar{q}')$, average surface temperature $(\bar{T}_s)$ and bulk fluid temperature (T_f) based on (10).

$$\bar{h} = \frac{\bar{q}'}{(\bar{T}_s - T_f)} \tag{10}$$

The area averaged values of heat transfer coefficient for surfaces of interest are calculated at the chosen location and the final results tabulated in Table V. The heat transfer coefficient for surfaces exposed to natural convection is assumed to be 10 W/m^2-K based on average values of data published in [15]. The heat transfer coefficient is then used to calculate the thermal resistances at the boundaries and used to build up the thermal conductance matrix $[K]$ in (1).

TABLE V
SUMMARY OF HEAT TRANSFER COEFFICIENT

Heat Transfer Coefficient	Values (W/m^2-K)	Heat Transfer Coefficient	Values (W/m^2-K)
h1	147	h6	10
h2	21	h7	39
h3	55	h8	70
h4	7	h9	38
h5	43	h10	13

3. Heat Generation

The heat generation at each element is derived from the loss model that has been developed for similar electromagnetic machines as presented by Gieras et. al. [4]. The main losses in such machines are the copper losses ($P_{l,c}$), eddy current losses ($P_{l,e}$) hysteresis losses ($P_{l,h}$) and mechanical losses ($P_{l,m}$). The resistive heating in the copper windings can be calculated from the phase to phase RMS current (I_{rms}) of the machine and the resistive property of copper based on Equation (11). R_o is the resistance of copper at 20°C while T_c is the temperature of the copper winding. The losses in the copper windings can therefore be calculated to a certain degree of accuracy.

$$P_{l,c} = 3R_o\big(1 + 0.00393(T_c - 20)\big)I_{rms}{}^2 \quad (11)$$

However, the eddy current and hysteresis losses are highly complex functions of material property, dimension and operating conditions. It is not within the scope of this paper to discuss in detail the formulation and intricacies of a complex issue. Nevertheless, it is in the interest of the reader that the basic relationship is presented so it is made clear what are the main factors affecting these losses.

The factors and their relationship to the losses are summarized by (12) and (13) respectively. B is a function of the harmonic component of the magnetic flux density raised to a power m or n which depends on how the magnetic flux density is derived. ω is the rotation speed of the rotor while a and c are correction factors for the geometry and material properties.

$$P_{l,e} \propto aB^m\omega^2 \quad (12)$$
$$P_{l,h} \propto cB^n\omega^2 \quad (13)$$

The mechanical loss ($P_{l,m}$) is the sum of the bearing losses ($P_{l,b}$) and windage losses ($P_{l,w}$). They can be described by the relationship in (14) and (15) respectively where M is the mass of the rotor and R is the radius of the rotor. The total loss for the whole machine (P_l) is obtained by summing all the losses as shown in (16). For the purpose of this work, the losses are calculated wherever possible but some are obtained from empirical correlations obtained from data collected during experimental testing.

$$P_{l,b} \propto M\omega \quad (14)$$
$$P_{l,w} \propto R^3\omega^5 \quad (15)$$
$$P_l = P_{l,c} + P_{l,e} + P_{l,h} + P_{l,b} + P_{l,w} \quad (16)$$

With all the necessary input to the model predetermined, (1) can be solved to obtain the temperature distribution. Instead of solving the set of coupled first order differential equation for an exact solution, the equation can be discretised using a forward difference method in time. The discretised form is given by (17) .

$$\{T^{n+1}\} = \{T^n\} + \delta t[C]'\langle[K]\{T^n\} + \{P_l\}\rangle \quad (17)$$

A time step (δt) equal to 0.1 seconds is chosen to ensure the convergence of the solution. Equation (17) can then be solved explicitly because the temperature of the next iteration $\{T^{n+1}\}$ depends only on the temperature of the current iteration $\{T^n\}$. Equation (17) is solved iteratively to obtain the time response of the temperature with a prescribed initial condition [16].

III. Experimental Testing and Results

The test case that is performed on the EVO AFM140 is based on a set up where the machine is running in motor mode. The input to the system is a 3 phase AC voltage which produces the current to meet the torque demand. The target torque is set at a continuous torque of 160 Nm for 120 seconds. The motor controller is designed to regulate the voltage and current supplied to the machine to achieve the set torque. The rotation speed of the motor is set at 2000rpm and thus the theoretical power output from the machine is about 33.5 kW in this set up.

The heat generation due to the losses as discussed earlier causes the temperature of the machine to rise. The temperature is measured at several points which include one point at the end windings, the inner region of the casing and outer region of the casing. The temperature at the end winding is measure using a Class B Platinum Resistance Thermometer (PRT) while K type thermocouples are used for measurements at the casings. The instruments have a measuring accuracy of ± 0.5 °C and ± 1.5 °C respectively for the current range of measurement. The data is recorded on a National Instrument data acquisition system at a sample rate of 0.5Hz. The temperature variations as measured in the experiments are shown in Fig. 8. The maximum temperature recorded for this test is 48.5 °C at the end windings.

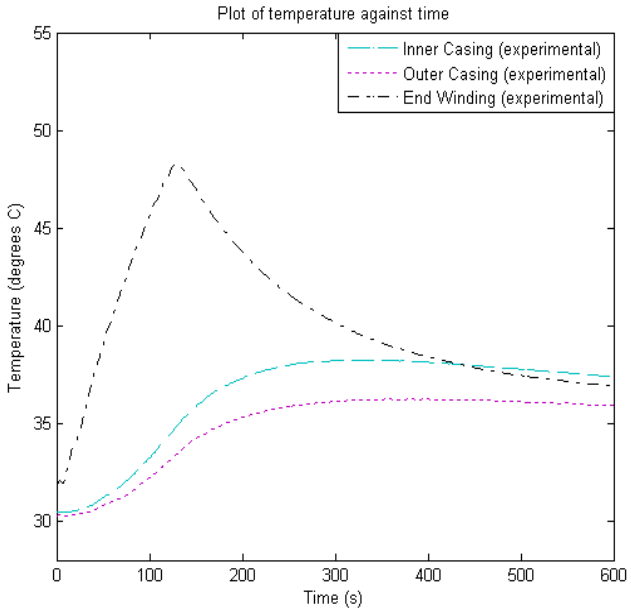

Fig. 8 Temperature variation with time (experimental)

A simulation of the machine temperature is done using the hybrid model presented earlier. The operating conditions are as per the experiment and it is used as an input to estimate the amount of losses generated. The simulation is allowed to run for a total time of 600s to obtain temperature data for comparison with the experimental data as shown in Fig. 9.

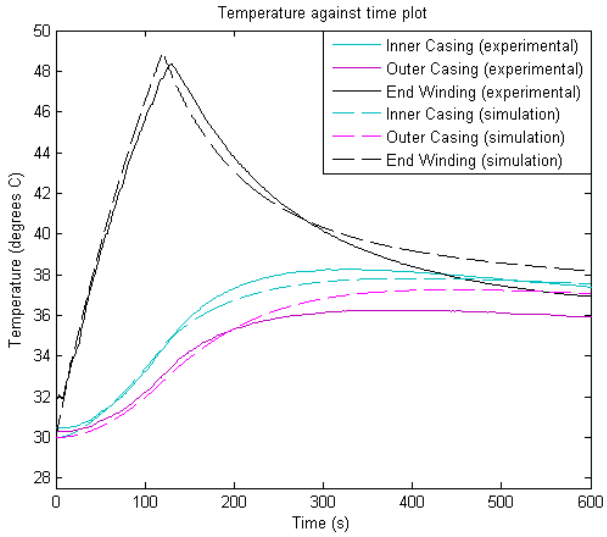

Fig. 9 Experimental and simulated temperature variation

The temperature prediction of the model is reasonably accurate as shown by the dashed line in Fig. 9. The general trend of the temperature is in good agreement with the experimental data. The shape of the curve is characteristic of a first order system where the time constant can be easily calculated. The exponential increase and decrease can be observed in the heating and cooling phase respectively.

To do a systematic comparison, the measured temperatures for the individual measurement points are plotted against the simulated temperature. The percentage error of the simulated temperature is calculated for each point of measurement at each interval of the time step. The percentage error is calculated using (18) and plotted in Fig. 10.

$$e_{\%} = \frac{|T_{sim} - T_{exp}|}{T_{exp}} \, x \, 100\% \qquad (18)$$

The largest error is recorded for the simulated temperature at the end winding. The model has overestimated the temperature by about 3.4 %. The maximum error recorded at the inner casing and outer casing is about 1.7 % and 3.2 % respectively. The mean error in temperature prediction for the end winding, inner casing and outer casing are about 2.0 %, 0.8 % and 1.8 % respectively. The error in temperature prediction is plotted (dashed line) against the measurement error due to the uncertainty of the measurement device (solid line) in the error plot in Fig. 10. The error in temperature prediction is consistently lower than the measurement error on average. The summary of the error in temperature prediction is tabulated in Table VI.

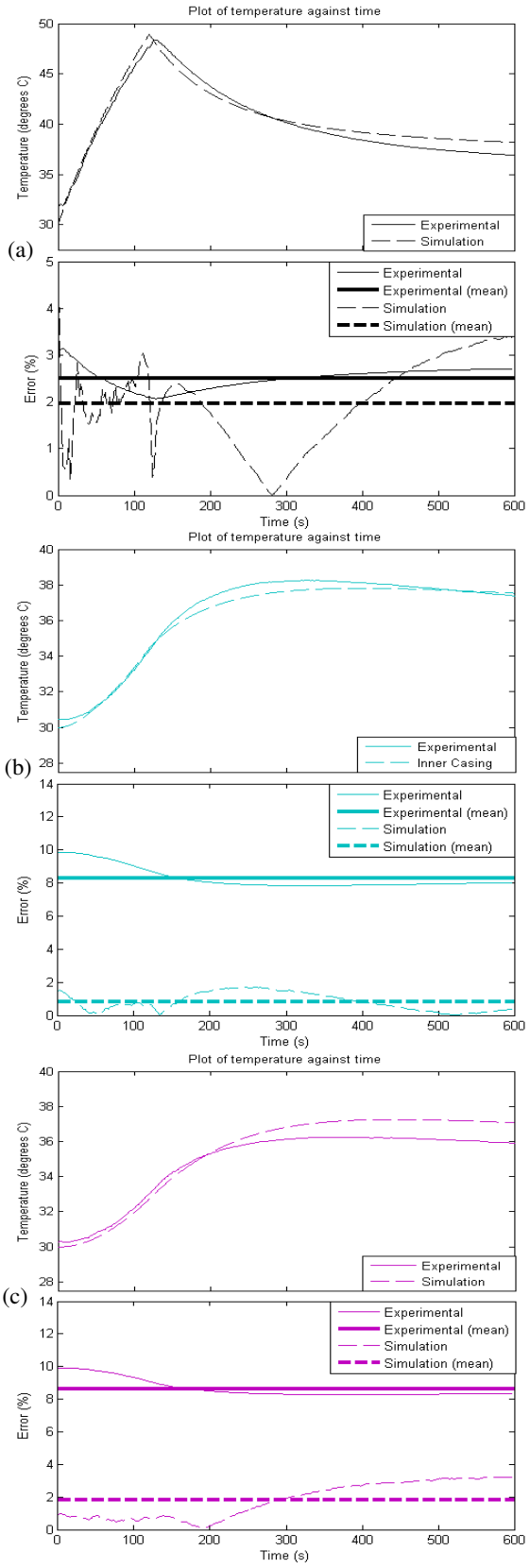

Fig. 10 Experimental and simulated temperature with corresponding error for (a) end winding, (b) inner casing and (c) outer casing

TABLE VI
SUMMARY OF ERROR

Location	Mean error (experimental)	Mean error (simulation)
End Winding	2.5 %	2.0 %
Inner Casing	8.3 %	0.8 %
Outer Casing	8.6 %	1.8 %

In order to make a comparison of the rate of temperature change, the time constant for the heating path can be calculated for both the experimental and simulation data. The summary of the time constant is shown in Table VII. There is good agreement between the experimental and simulation data for the rate of temperature change as described by the time constant. The maximum error for the time constant prediction is about 13.3%.

TABLE VII
SUMMARY OF TIME CONSTANT AND ASSOCIATED ERROR

	Experimental	Simulation	% error
End Winding (heating)	74 s	71s	4.1%
Inner casing (heating)	142 s	138s	2.8%
Outer casing (heating)	158 s	179 s	13.3%

IV. DISCUSSION

The temperature prediction of the model is in good agreement with the measured temperature. As expected, the highest temperature is recorded at the end windings. This is because most of the heat is generated here and there is little mechanism of heat transfer due to the high thermal contact resistance of the insulation material as well as the re-circulating air pocket around it.

The rate of increase in temperature is fastest where the source of heat generation is located, as temperature is a function of time and space. As such, the time constant for the heating path is much faster in the windings than in the other parts of the machine. The exact parameter affecting the time constant is a complex function of thermal conductivity, heat transfer coefficient, contact area and the general path of heat transfer. These parameters are interrelated as they are coupled together in the thermal conductivity matrix [*K*] in (1) and they affect the temperature distribution of the entire machine though with different impact.

Convection heat transfer is generally less effective than heat transfer by conduction. The extent of convection heat transfer depends largely on, the surface area exposed to the fluid, its temperature and the extent of forced convection. To illustrate the effect of the convective heat transfer, the temperature of the end windings, casing and magnet are simulated using the model. Two different cases are chosen to show the effect of convective cooling on different components. In the first case, the motor is simulated to be running at 2000 rpm with a voltage and current input to produce 160 Nm of torque for 120s. The rotation of the rotor causes forced convection on the components. The second case has an equivalent input of the same duration but there is no rotation in this case. This means there is less cooling due to the absence of forced fluid motion.

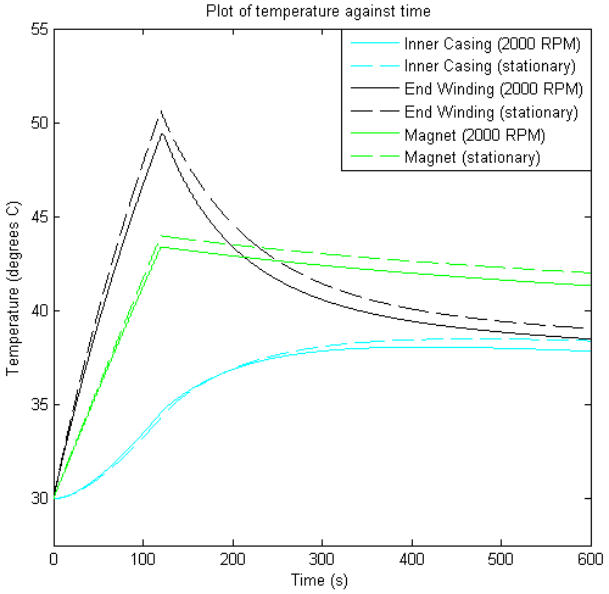

Fig. 11 Temperature variation due to convection cooling caused by rotor motion

The temperature of the end windings, casing and magnet decreases as the convection cooling effect is enhanced due to rotor motion as shown in Fig. 11. The reduced temperature shows that the rotor motion indeed enhances the heat transfer to and from the fluid. The end winding, inner casing and magnet temperature recorded a reduction of 2.2%, 1.4% and 1.1% in temperature respectively because of rotor motion. The rotor motion does help in reducing the temperature of the machine in general. However, the effect of convection heat transfer may be less than reducing the thermal resistance of the heat conduction path.

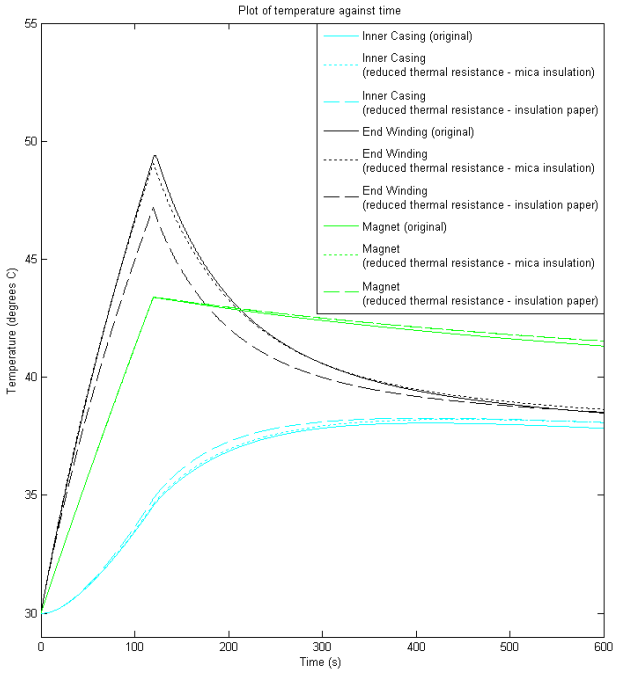

Fig. 12 Temperature variation of the casing, end winding and magnet for thermal barriers with different thermal resistances

The temperature variation of the machine is most sensitive to the thermal resistances of materials that are limiting the heat transfer. Based on the experimental data, the large difference in temperature between the end windings and stator shows that there is a high thermal resistance across the path connecting the two components. The first thermal barrier would be the mica insulation layer around each copper winding and the second thermal barrier would be the insulation paper around the whole bundle of copper winding.

Fig. 12 shows the effects of halving the thermal resistances of the mica insulation (dotted line) and insulation paper (dashed line). The maximum temperature recorded at the three points of interest shows a much larger change when the thermal resistance of the insulation paper is halved. The maximum temperature is reduced by 4.6% at the end windings while the casing registered an increase in temperature of 0.5%. On the other hand, the change in maximum temperature when the thermal resistance of the mica insulation is halved shows little change at all. This observation points to the fact that the final temperature of the machine is largely dependent on the limiting thermal barriers. In this case, the limit in heat transfer is at the insulation paper. Thus, any change in the thermal resistance of this barrier would result in an appreciably larger change in temperature.

V. Conclusion

It can be seen from the results that the model is able to predict the temperature of the machine accurately with a maximum error of 3.4% and the average error for all three measurement points do not exceed 3% which is equivalent to the minimum error due to the measurement device for the range of temperature measured. In other words, the model is able to predict the temperature of the machine within the acceptable experimental error margin.

The hybrid thermal model also allows for greater flexibility in terms of the choice of the size and shape of elements. It can follow the physical shape of the components for greater accuracy with fewer elements. This increase in accuracy is not at the expense of increasing computational time because of the finer elements that is generally required in Finite Element (FE) methods to increase accuracy.

The hybrid thermal model is described by a set of coupled linear first order differential equations which can be easily discretised and solved to obtain the temperature. The simplicity of the mathematical model allows for fast computation which is essential for transient temperature prediction. As such the hybrid thermal model developed here is suitable for transient temperature prediction of the AFM140 AFPM machine and indeed it could be implemented to other similar AFPM machines.

Acknowledgment

The author would like to thank the management and staff of EVO Electric for their support of this project which was critical to the success of the publication of this work. The use of the test rig and equipment at EVO Electric was essential in obtaining the experimental data. The invaluable technical support from the staff at EVO Electric especially Adam Malloy and Dr. Malte Jaensch is greatly appreciated. My appreciation also goes out to those who have helped in this project in one way or another.

References

[1] K. Sitapati and R. Krishnan, "Performance comparisons of radial and axial field, permanent-magnet, brushless machines," *IEEE Transactions on Industry Applications*, vol. 37, 2001, pp. 1219-1226.

[2] M.U. Lamperth, a Beaudet, and M. Jaensch, "Disc motors for automotive applications," *Hybrid & Eco Friendly Vehicles Conference 2008 (HEVC 2008)*, 2008, pp. 10-10.

[3] H. Auinger, "Efficiency of electric motors under practical conditions," *Power Engineering Journal*, vol. 15, 2001, p. 163.

[4] J.F. Gieras, *Axial Flux Permanent Magnet Brushless Machines*, 2008.

[5] S. Scowby, "Thermal modelling of an axial flux permanent magnet machine," *Applied Thermal Engineering*, vol. 24, Feb. 2004, pp. 193-207.

[6] T. Sebastian, "Temperature effects on torque production and efficiency of PM motors using NdFeB magnets," *IEEE Transactions on Industry Applications*, vol. 31, 1995, pp. 353-357.

[7] A. Boglietti, A. Cavagnino, D. Staton, M. Shanel, M. Mueller, and C. Mejuto, "Evolution and Modern Approaches for Thermal Analysis of Electrical Machines," *IEEE Transactions on Industrial Electronics*, vol. 56, Mar. 2009, pp. 871-882.

[8] D. Staton, a Boglietti, and a Cavagnino, "Solving the More Difficult Aspects of Electric Motor Thermal Analysis in Small and Medium Size Industrial Induction Motors," *IEEE Transactions on Energy Conversion*, vol. 20, Sep. 2005, pp. 620-628.

[9] P.H. Mellor, D. Roberts, and D.R. Turner, "Lumped parameter thermal model for electrical machines of TEFC design," *IEE Proceedings B Electric Power Applications*, vol. 138, 1991, p. 205.

[10] C.H. Lim, G. Airoldi, J.R. Bumby, R.G. Dominy, G.I. Ingram, K. Mahkamov, N.L. Brown, a Mebarki, and M. Shanel, "Experimental and CFD investigation of a lumped parameter thermal model of a single-sided, slotted axial flux generator," *International Journal of Thermal Sciences*, vol. 49, Sep. 2010, pp. 1732-1741.

[11] E. Odvárka, N.L. Brown, A. Mebarki, M. Shanel, S. Narayanan, and C. Ondrusek, "Thermal modelling of water-cooled axial-flux permanent magnet machine," *5th IET International Conference on Power Electronics, Machines and Drives (PEMD 2010)*, 2010, pp. 1-5.
[12] M. Tari, K. Yoshida, S. Sekito, J. Allison, R. Brutsch, a Lutz, and N. Frost, "A high voltage insulating system with increased thermal conductivity for turbo generators," *Proceedings: Electrical Insulation Conference and Electrical Manufacturing and Coil Winding Technology Conference (Cat. No.03CH37480)*, 2001, pp. 613-617.
[13] E. Serre, P. Bontoux, and B. Launder, "Transitional-turbulent flow with heat transfer in a closed rotor-stator cavity," *Journal of Turbulence*, vol. 5, Feb. 2004.
[14] D. a Howey, a S. Holmes, and K.R. Pullen, "Radially resolved measurement of stator heat transfer in a rotor–stator disc system," *International Journal of Heat and Mass Transfer*, vol. 53, Jan. 2010, pp. 491-501.
[15] D.P. DeWitt, *Fundamentals of heat and mass transfer*, 1996.
[16] J. Nerg, M. Rilla, and J. Pyrhonen, "Thermal Analysis of Radial-Flux Electrical Machines With a High Power Density," *IEEE Transactions on Industrial Electronics*, vol. 55, Oct. 2008, pp. 3543-3554.